Investigation of iron containing intermetallics in AlSi12 alloy with w (Mn/Fe) = 0.99

(Univerza u Ljubljani Naravoslovnotehniška faulteta, Mosdorfer GmbH, Weiz, Austrija) Kozina, Franjo; Zovko Brodarac, Zdenka; Drobnjak, Dalibor; Jukić, Ivan

Permanent link / Trajna poveznica: https://urn.nsk.hr/urn:nbn:hr:115:741358

Download date / Datum preuzimanja: **2024-04-20**

Repository / Repozitorij:

Repository of Faculty of Metallurgy University of Zagreb - Repository of Faculty of Metallurgy University of Zagreb

INVESTIGATION OF IRON CONTAINING INTERMETALLICS IN AlSi12 ALLOY WITH w (Mn/Fe) = 0.99

Franjo Kozina[1*], Zdenka Zovko Brodarac[1], Dalibor Drobnjak[2], Ivan Jukić[3]

[1] University of Zagreb Faculty of Metallurgy, Sisak, Croatia
[2] Almos Ltd, Kutina, Croatia
[3] Mosdorfer GmbH, Weiz, Austria

Abstract

The precipitation of iron-rich intermetallic phases in AlSi12 alloy with manganese/iron weight ratio w (Mn/Fe) = 0.99 was investigated. Calculation of solidification sequence under equilibrium conditions, obtained using Computer Aided Thermodynamic Diagram Calculation, comprehended precipitation of α-Al$_{15}$(FeMn)$_3$Si$_2$ and β-Al$_5$FeSi. However, the microstructural investigations performed using light and electron microscopy indicated the lack of β-Al$_5$FeSi in needle-like morphology. The intermetallic phases in Chinese script, transitional and polyhedral morphology were found, respectively. The results of Energy Dispersive Spectroscopy showed the minimum difference in the chemical composition between the intermetallic phases in Chinese script and polyhedral morphology due to high w (Mn/Fe) weight ratio.

Keywords: AlSi12, solidification sequence calculation, morphology of iron-rich intermetallic phases, w (Mn/Fe) ratio

*Corresponding author (e-mail address): fkozin@simet.hr

INTRODUCTION

The mechanical properties and development of microstructural constituents during solidification of aluminum-silicon (Al-Si) cast alloys are the result of chemical composition, melt treatment conditions, solidification rate [1], casting processes [2] and the application of, or the lack of, thermal treatment [3]. Chemical composition is designed in order to produce required performance capabilities including good specific strength and stiffness, low density, wear resistance, high temperature strength and improved damping capacity.

Interactions between alloying elements [4] promote development of microstructural constituents and affect solid solution of the matrix [5]. The alloying elements are classified as major or minor alloying elements and impurities, respectively [6]. Silicone, copper and magnesium are major alloying elements that control castability and properties development. Silicone is responsible for good castability, low density and abrasion resistance. While copper additions affect strength and hardness of Al-Si cast alloys, magnesium provides strength and corrosion resistance [6]. As minor alloying elements, titanium, boron, strontium, beryllium, manganese and chromium, influence solidification behavior, modify eutectic structure, refine primary phases and grain size morphology, promote or suppress phase formation and reduce oxidation [5]. Iron and zinc are impurity elements that can be partially dissolved into a solid solution of the matrix or form insoluble intermetallic phases. However, they are not homogeneously distributed between solid solution and intermetallic phases [6]. Besides impurities, the form and distribution of insoluble intermetallic phases is controlled by the addition of silicone, magnesium and copper [7]. In Al-Si-Mg alloys, zinc promotes precipitation at the grain boundaries increasing alloy susceptibility to stress corrosion cracking and crack propagation [8].

A major impurity element in Al-Si cast alloys that promotes intermetallic phase precipitation is iron. The iron is frequently acquired at levels of 0.4 wt. % to 0.8 wt. % during melting and casting processes [9], particularly when aluminum scrap and recycled materials are used [10]. Although the presence of iron prevents die soldering in high pressure die casting [11], the excess amount of iron has been found detrimental for mechanical properties of Al-Si, Al-Si-Cu and Al-Si-Mg cast alloys [12]. In order to avoid soldering effect and production of defect castings with short end of life [13], the iron must be maintained at or above its saturation point in the liquid aluminum [14]. However, the reduction of iron content in cast Al-alloys is necessary, due to the precipitation of Fe-rich intermetallic phases. The effect of Fe-rich intermetallic phases on the mechanical properties of cast Al-alloys depend on their type, size and distribution in the microstructure [15].

Although iron is highly soluble in liquid aluminum (L) and its alloys, it has a low solubility in aluminum solid solution (α_{Al}) of 0.052 wt. %. As a result iron tends to form intermetallic phases of various types. Equilibrium solubility of iron in L can reach 2.5 wt. % at a melting temperature of 700 °C and up to 5 wt. % at 800 °C [16].

Equilibrium Al-Fe phase diagram is characterized by eutectic interaction between the α_{Al} and stable Al_3Fe phase [16]. However, at higher cooling rates, due to the increased supercooling and changes in nucleation and growth conditions, precipitation of metastable phases is expected. Al-rich corner of stable and metastable Al-AlFe phase diagram is given in Figure 1. The metastable phases that precipitate in Al-Fe system are Al_xFe (Al_6Fe) [17] and Al_mFe (Al_9Fe_2) [18], respectively.
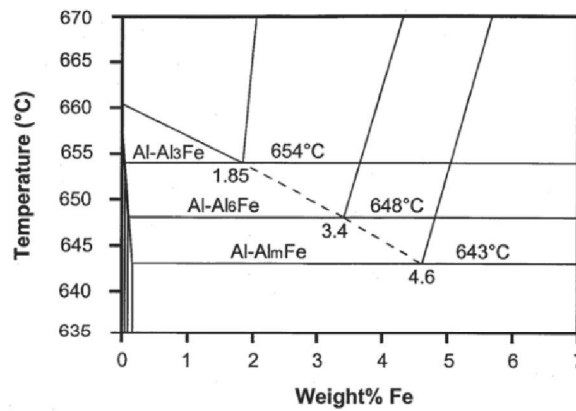
Figure 1. Al-rich corner of the stable and metastable Al-AlFe phase diagram [19]

The stable Al_3Fe phase solidifies at 1.85 wt. % Fe and 655 °C (Figure 1). At the commercial cooling rates of $10^{-1} - 10^2$ K/s the solidification of stable and metastable phases occurs. The cooling rate of $10^{-1} - 10$ K/s promotes solidification of Al_6Fe intermetallic phase at 3.4 wt. % Fe and 648 °C (Figure 1). The metastable Al_9Fe_2 phase precipitates at 4.6 wt. % Fe and 643 °C with cooling rate of 20 K/s [19] (Figure 1).

Thermodynamic description of Al-Fe-Si phase diagram comprehends solidification of eutectic $(\alpha_{Al} + \beta_{Si})$, α_{Al}, as well as Al_3Fe, α-Al_8Fe_2Si, β-Al_5FeSi, γ-Al_3FeSi and δ-Al_4FeSi_2 intermetallic phases [20].

The liquidus projection of the Al - corner of the Al-Fe-Si system is given in Figure 2. The corresponding invariant reactions are given in Table 1.
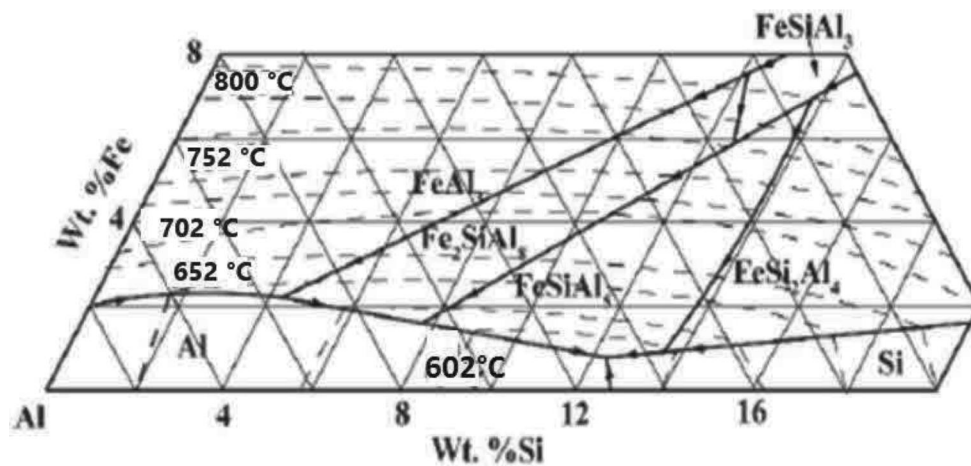

Figure 2. Liquidus projection in the Al corner of Al-Fe-Si ternary phase diagram [20]

Table 1. Invariant equilibrium reactions in the Al corner of Al-Fe-Si phase diagram [22]

Reaction No.	Reaction	Concentration in liquid phase, wt. %		Temperature, °C
		Fe	Si	
1	$L + Al_3Fe \rightarrow \alpha\text{-}Al_8Fe_2Si + \Upsilon\text{-}Al_3FeSi$	7.5	12.5	710
2	$L + \Upsilon\text{-}Al_3FeSi + \delta\text{-}Al_4FeSi_2 \rightarrow \beta\text{-}Al_5FeSi$	7.2	14.0	700
3	$L + \Upsilon\text{-}Al_3FeSi \rightarrow \alpha\text{-}Al_8Fe_2Si + \beta\text{-}Al_5FeSi$	6.0	13.0	675
4	$L + Al_3Fe \rightarrow \alpha_{Al} + \alpha\text{-}Al_8Fe_2Si$	2.0	4.2	632
5	$L + \alpha\text{-}Al_8Fe_2Si \rightarrow \alpha_{Al} + \beta\text{-}Al_5FeSi$	1.8	6.2	613
6	$L + \delta\text{-}Al_4FeSi_2 \rightarrow \beta\text{-}Al_5FeSi + \beta_{Si}$	1.5	14.3	600
7	$L \rightarrow \alpha_{Al} + \beta\text{-}Al_5FeSi + \beta_{Si}$	0.5	11.7	573

Based on the liquidus projection of Al-rich corner given in Figure 2, eutectic ($\alpha_{Al} + \beta_{Si}$), α_{Al}, Al_3Fe, $\alpha\text{-}Al_8Fe_2Si$, $\beta\text{-}Al_5FeSi$, $\Upsilon\text{-}Al_3FeSi$ and $\delta\text{-}Al_4FeSi_2$ are in equilibrium with L [23].

According to the Table 1, $\alpha\text{-}Al_8Fe_2Si$ and $\Upsilon\text{-}Al_3FeSi$ intermetallic phases are the first to solidify during peritectic reaction between L and Al_3Fe phase at 710 °C (reaction no. 1). The solidification of $\Upsilon\text{-}Al_3FeSi$ phase introduces a partial disorder to the α_{Al} dendritic network due to the partial substitution of aluminum and silicone atoms. The partial substitution of atoms is a result of large homogeneity of $\Upsilon\text{-}Al_3FeSi$ phase [24]. Solidification of $\beta\text{-}Al_5FeSi$ at 700 °C involves peritectic reaction of L, $\Upsilon\text{-}Al_3FeSi$ and $\delta\text{-}Al_4FeSi_2$ phase (reaction no. 2). Dissolution of previously precipitated $\Upsilon\text{-}Al_3FeSi$ and $\delta\text{-}Al_4FeSi_2$ phases increases the amount of silicone in L from 12.5 wt. % to 14.0 wt. %. The amount of silicone in L still remains high (13 wt. %) at 675 °C during solidification of $\alpha\text{-}Al_8Fe_2Si$ and $\beta\text{-}Al_5FeSi$ phase. At this stage solidification of $\alpha\text{-}Al_8Fe_2Si$ and $\beta\text{-}Al_5FeSi$ phase involves dissolution of $\Upsilon\text{-}Al_3FeSi$ (reaction no. 3). Transformation of α_{Al} dendritic network starts at 632 °C parallel to solidification of $\alpha\text{-}Al_8Fe_2Si$ phase (reaction no. 4). This reaction causes significant drop of silicone in L phase from 13 wt. % to 4.2 wt. %. The silicone content in L increases to 6.2 wt. % during solidification of $\beta\text{-}Al_5FeSi$ at 613 °C (reaction no. 5). The increase in silicone content from 6.2 wt. % to 14 wt. % if followed by solidification of $\beta\text{-}Al_5FeSi$ and primary β_{Si} (reaction no. 6) from silicone bulked L. The sequence ends with solidification of eutectic ($\alpha_{Al} + \beta_{Si} + \beta\text{-}Al_5FeSi$) at 573 °C (reaction no. 7).

The solid solubility of iron and silicone in α_{Al} related to temperatures is given in Figure 3. The solid solubility of iron and silicone in α_{Al} is indicated in Table 2.
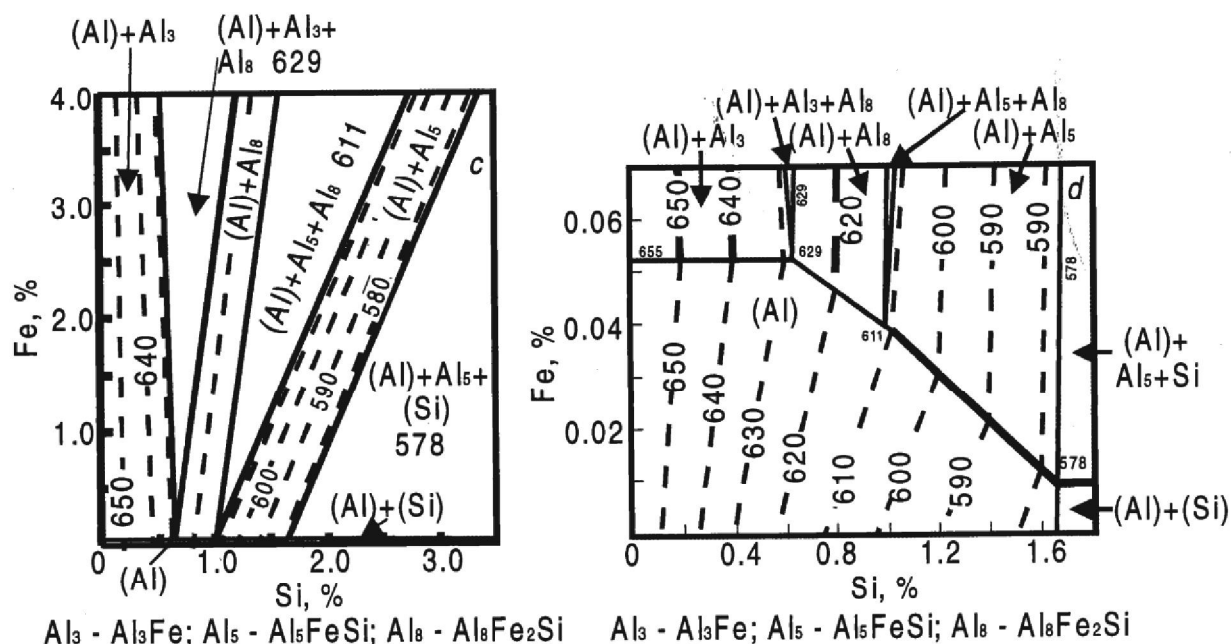
Figure 3. Solidus projection of primary iron intermetallic phases [25]

Table 2. Solid solubility of iron and silicone in α_{Al} at different temperatures [25]

T, °C	α_{Al} + Al$_3$Fe + α-Al$_8$Fe$_2$Si		α_{Al} + β-Al$_5$FeSi + α-Al$_8$Fe$_2$Si		α_{Al} + β-Al$_5$FeSi + β$_{Si}$	
	Fe, wt. %	Si, wt. %	Fe, wt. %	Si, wt. %	Fe, wt. %	Si, wt. %
629	0.052	0.64	--	--	--	--
611	--	--	0.040	0.82	--	--
600	0.033	0.40	0.033	0.82	--	--
550	0.0016	0.20	0.016	0.42	0.008	1.30
400	0.002	0.03	0.002	0.06	0.002	0.30

Based on the solidus projection of Al-rich corner in Al-Fe-Si phase diagram, Al$_3$Fe, α-Al$_8$Fe$_2$Si, β-Al$_5$FeSi and eutectic (α_{Al} + β$_{Si}$) are in equilibrium with α_{Al} dendritic network (Figure 3) [26].

When silicone content in solid solution is 0.64 wt. %, Al$_3$Fe and α-Al$_8$Fe$_2$Si phase solidify at 629 °C (Figure 3). Increasing silicone content to 0.83 wt. % causes solidification of ternary β-Al$_5$FeSi and α-Al$_8$Fe$_2$Si phase at 611 °C. The eutectic (α_{Al} + β$_{Si}$ + β-Al$_5$FeSi) solidify at 590 °C and silicone content of 1.20 wt. % [25].

Taking into account phase transformation and solidification in liquid and solid state (Table 1 and 2), there are five main Fe-rich intermetallic phases: Al$_3$Fe, α-Al$_8$Fe$_2$Si, β-Al$_5$FeSi, ϒ-Al$_3$FeSi and δ-Al$_4$FeSi$_2$. Solidification of Fe-rich intermetallic phases originates from low solubility of iron in α_{Al} solid solution. The δ-Al$_4$FeSi$_2$ phase solidifies in aluminum alloys with silicone content of 14 wt. %, while ϒ- Al$_3$FeSi phase is present in alloys with high silicone (12.5 wt. %) and iron (7.5 wt.%) content [27]. The thermodynamic stability of α-Al$_8$Fe$_2$Si phase is only achieved in high purity Al-Fe-Si alloys. The presence of other alloying elements, such as

manganese, chromium [28] and vanadium, introduce changes into the lattice of α-Al$_8$Fe$_2$Si phase [29]. The changes in lattice of α-Al$_8$Fe$_2$Si phase originate from iron and alloying element substitution as well as mutual substitution of silicone and aluminum [30]. The β-Al$_5$FeSi intermetallic phase solidifies during pre-eutectic reaction in liquid/solid range [31]. The brittle β-Al$_5$FeSi intermetallic phase has needle-like or plate-like morphology [32]. This type of morphology acts as a crack initiator and has a negative effect on mechanical properties [33] as well as on castability [34]. Poor castability originates from increased content of porosities. The β-Al$_5$FeSi intermetallic phase increases the porosity content by blocking dendritic flow and therefore acting as a nucleation site [35]. Also β-Al$_5$FeSi intermetallic phase enables growth of large Al-Si eutectic grains [36].

Neutralizing negative effect of β-Al$_5$FeSi intermetallic phase comprehends modification of its needle-like morphology to less deleterious form of Chinese script. Neutralizing effect is achieved by adding soluble neutralizer elements such as manganese, chromium, beryllium or strontium [37]. Manganese is the most frequent neutralizing element [38] that promotes precipitation of α-Al$_{15}$(FeMn)$_3$Si$_2$ phase [27] during peritectic reactions [39]. Precipitation of β-Al$_5$FeSi intermetallic phase is suppressed, respectively. The invariant equilibrium reactions in Al-rich corner of Al-Fe-Mn-Si diagram are given in Table 3.

Table 3. The invariant equilibrium reactions in Al-rich corner of Al-Fe-Mn-Si diagram [25]

Reaction	Composition of Liquid			Temperature, °C
	Fe, wt. %	Mn, wt. %	Si, wt. %	
L + Al$_3$Fe +Al$_6$(FeMn) → α$_{Al}$ + α-Al$_{15}$(FeMn)$_3$Si$_2$	2.0	0.35	1.75	648
L + Al$_3$Fe → α$_{Al}$ + α-Al$_8$Fe$_2$Si + α-Al$_{15}$(FeMn)$_3$Si$_2$	2.0-2.5	<0.2	3.0-5.0	627-632
L + α-Al$_8$Fe$_2$Si → α$_{Al}$ + β-Al$_5$FeSi + α-Al$_{15}$(FeMn)$_3$Si$_2$	1.0-2.0	0.1-0.5	5.0-10.0	597-607
L + β-Al$_5$FeSi → α$_{Al}$ + β$_{Si}$ + α-Al$_{15}$(FeMn)$_3$Si$_2$	0.6	0.2	11.7	575

According to Table 3, transformation of α$_{Al}$ dendritic network and solidification of α-Al$_{15}$(FeMn)$_3$Si$_2$ phase are first reactions to occur. Their solidification is a result of peritectic reaction between L, Al$_3$Fe and Al$_6$(FeMn) phase at 648 °C. The transformation of α$_{Al}$ dendritic network and solidification of α-Al$_{15}$(FeMn)$_3$Si$_2$ phase are continuous till the end of liquid state reactions. In the temperature range from 627 °C to 632 °C, primary α-Al$_8$Fe$_2$Si phase begins to solidify. The solidification of primary α-Al$_8$Fe$_2$Si enables peritectic reaction, in the temperature range from 597 °C to 607 °C and solidification of β-Al$_5$FeSi. Liquid state reactions end with transformation of α$_{Al}$ dendritic network, solidification of eutectic (α$_{Al}$ + β$_{Si}$) and α-Al$_{15}$(FeMn)$_3$Si$_2$. The solidification of eutectic (α$_{Al}$ +β$_{Si}$) is a result of increased amount of silicone in L. The eutectic (α$_{Al}$ +β$_{Si}$) solidifies at 11.7 wt. % of silicone. The amounts of iron and manganese in L decrease towards the end of liquid state reactions (Table 3), respectively.

The Al$_6$Mn, eutectic (α$_{Al}$ + β$_{Si}$) and α-Al$_{15}$(FeMn)$_3$Si phases are in equilibrium with α$_{Al}$ solid solution. In the α-Al$_{15}$(FeMn)$_3$Si phase, iron can replace up to 90 % of manganese. The metastable Al$_6$Fe and Al$_{20}$Fe$_5$Si$_2$ phase only occur in rapidly quenched alloys [40].

The solidification of Fe-rich intermetallic phase can occur in different morphologies: needle-like, Chinese script and polyhedral or star-like morphology. The morphology of precipitated phases is influenced by manganese/iron weight ratio (w (Mn/Fe)). The exact w (Mn/Fe) necessary for neutralizing effect of manganese and the transition of needle-like to Chinese script morphology is not fully established. With the w (Mn/Fe) at 0.35 the partial transformation of needle-like to Chinese script morphology was observed. At w (Mn/Fe) of 0.5 transformation of β-Al$_5$FeSi to α-Al$_{15}$(FeMn)$_3$Si$_2$ was fully achieved [41]. However, α - Al$_{15}$(FeMn)$_3$Si$_2$ with Chinese script morphology was observed at w (Mn/Fe) as low as 0.17 [27]. Increasing the w (Mn/Fe) additionally causes precipitation of α-Al$_{15}$(FeMn)$_3$Si$_2$ with polyhedral morphology. The precipitation of α-Al$_{15}$(FeMn)$_3$Si$_2$ phase with polyhedral morphology occurs at w (Mn/Fe) of 0.65 [41].

The goal of the research is to identify the Fe-rich intermetallic phases during solidification of AlSi12 alloy with w (Mn/Fe) of 0.99.

MATERIALS AND METHODS

The AlSi12 alloy was prepared in induction melting furnace from the ingot and return material. After melting at the temperature of 770 °C the melt treatment was performed through inoculation with AlTi5B master alloy and modification with AlSr10 master alloy. High-pressure die casting was used. The chemical composition was determined spectroscopically using Spectro machine.

The calculations of Fe-rich intermetallic phase development under equilibrium conditions were enabled using CALPHAD. The CALPHAD enabled calculation of aluminum, iron, silicone and manganese interaction with bulked α$_{Al}$ as well as solidification sequence calculations and reactions in both liquid and solid state, respectively.

Samples for metallographic analysis were prepared using grinding/polishing machine Pheonix Beta Biller SAD. In order to observe microstructural constituents, samples were etched using Keller's etching solutions as well as caustic chemical etching. The caustic chemical etching was performed using 30 % aqueous solution of sodium hydroxide (NaOH) and 0.1 M hydrochloric acid (HCl). The application of caustic chemical etching enabled dissolution of α$_{Al}$ dendritic network. The rest of microstructural constituents were not affected. The Olympus GX51 inverted metallographic microscope was used to perform light microscopy. Electron microscopy was made on Tescan, Vega TS 5136 MM equipped with energy dispersive spectrometer (EDS). Backscatter electron (BSE) imaging was used in order to obtain better distinction between the elements based on atomic weight. The EDS measurements were performed on at least ten different details. Details for EDS measurements were determined based on phase morphology.

RESULTS AND DISCUSSION

The chemical composition of the casting is given in Table 4.

Table 4. Chemical composition of the casting, wt. %

Si	Fe	Cu	Mn	Mg	Cr	Ni	Zn	Ti	B	Bi
11.69	0.443	0.149	0.438	0.0250	0.011	0.011	0.0410	0.0270	0.003	0.0022

The AlSi12 alloy is hypoeutectic alloy with Si content of 11.69 wt. %. The w (Mn/Fe) is 0.99. The w (Mn/Fe) is sufficient to avoid solidification of β-Al$_5$FeSi intermetallic phase with needle-like morphology. Instead, the iron should solidify as α-Al$_{15}$(FeMn)$_3$Si$_2$ with Chinese script morphology. Given the w (Mn/Fe), solidification of α-Al$_{15}$(FeMn)$_3$Si$_2$ with polyhedral morphology is expected, as well. The additions of copper, chromium, nickel, zinc, titanium, boron and bismuth are higher than their solid solubility in α_{Al} dendritic network.

Phase transformation and precipitations under equilibrium conditions were determined using Thermo-Calc 2019a software support with TCAL 4 database. The thermodynamic calculations included elements from the chemical composition given in Table 4. The calculations concerning Fe-rich intermetallic phases as well as diffusion of aluminum, silicone, iron and manganese components were emphasized.

The amount of phases developed during solidification is given in Figure 4 a and b. The following reactions are shown in Table 5.
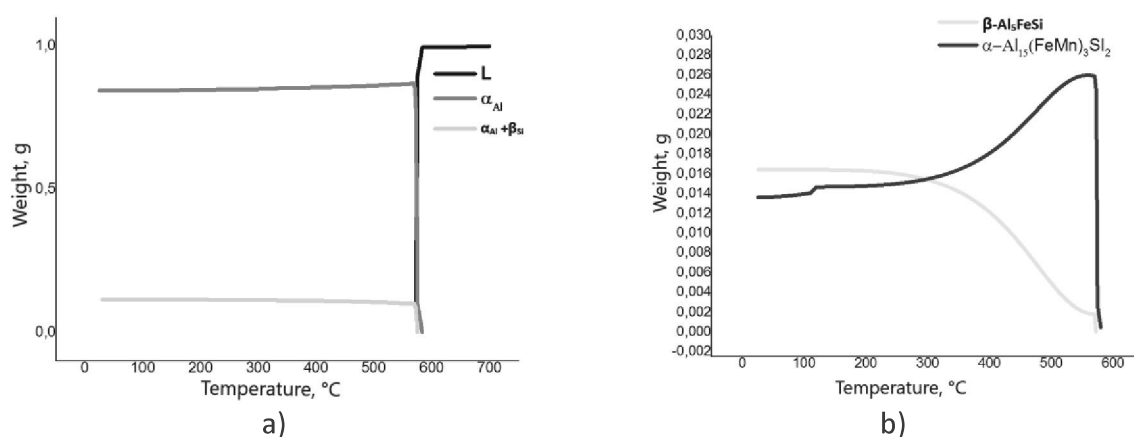

Figure 4. The amount of phases developed during solidification:
a) Transformation of α_{Al} dendritic network and solidification of eutectic (α_{Al} + β_{Si}),
b) Solidification of Fe-rich and α-Al$_{15}$(FeMn)$_3$Si$_2$ phase

Table 5. Solidification sequence according to Thermo-Calc calculations

Reaction no.	Reaction	Temperature, °C
1	L → α$_{Al}$	581
2	L + α$_{Al}$ → α-Al$_{15}$(FeMn)$_3$Si$_2$	580
3	L → α$_{Al}$ +β$_{Si}$	574
4	α$_{Al}$ + α-Al$_{15}$(FeMn)$_3$Si$_2$ → β-Al$_5$FeSi	570

The calculations of solidification sequence in equilibrium conditions comprehend solidification of α-Al$_{15}$(FeMn)$_3$Si$_2$ and β-Al$_5$FeSi. The solidification sequence begins with transformation of α$_{Al}$ dendritic network at 581 °C followed by solidification of α-Al$_{15}$(FeMn)$_3$Si$_2$ at 580 °C. The eutectic (α$_{Al}$ +β$_{Si}$) solidifies from L at 574 °C. The β-Al$_5$FeSi phase solidifies at 570 °C reducing the amount of α-Al$_{15}$(FeMn)$_3$Si$_2$ phase, respectively. The additional decrease in the amount of α-Al$_{15}$(FeMn)$_3$Si$_2$ phase occurs at 110 °C.

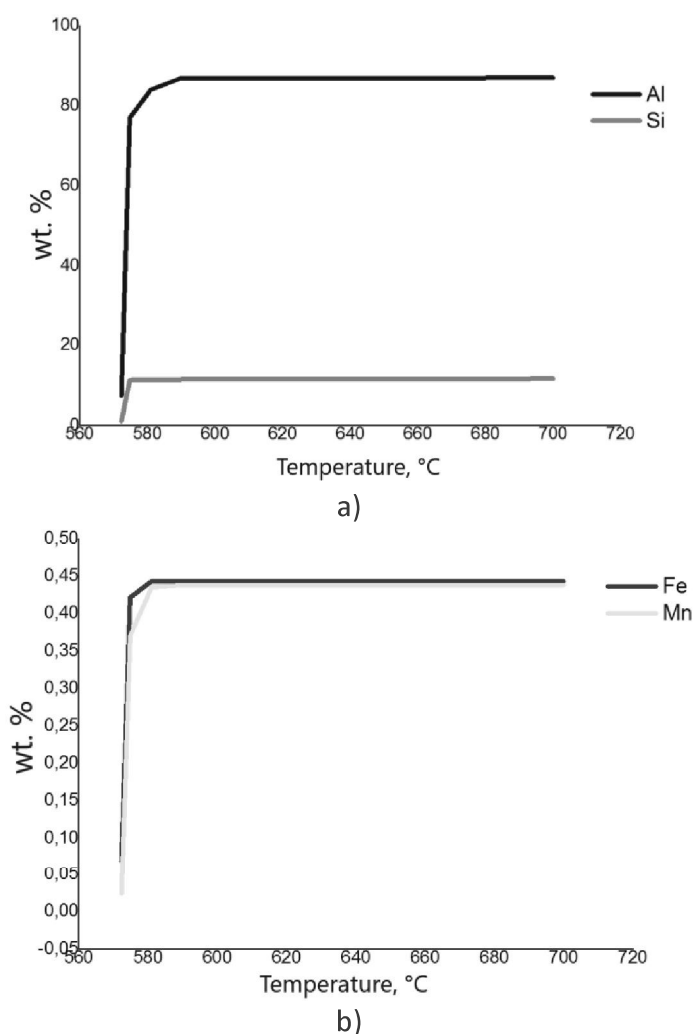The amount of components in L phase is given in Figure 5, a and b.

a)

b)

Figure 5. The component ratio in L: a) Al and Si, b) Fe and Mn

263

The average aluminum content of 86.88 wt. % in L phase stays constant till the temperature of 581 °C when it drops to 83.92 wt. % as α_{Al} dendritic network starts to transform. The solidification of eutectic ($\alpha_{Al} + \beta_{Si}$) reduces the amount of aluminum in L phase 574 °C when it reaches its minimum of 7.38 wt. %. The average silicone content of 11.63 wt. % in L phase drops at the 570 °C towards its minimum of 1.08 wt. % due to the solidification of eutectic ($\alpha_{Al} + \beta_{Si}$). The average content of iron and manganese follow the same pattern as aluminum. The significant drop in average content of manganese (0.44 wt. %) is recorded at the temperature of 580 °C as a result of α-$Al_{15}(FeMn)_3Si_2$ phase solidification, while average Fe content (0,44 wt. %) drops at the temperature of 570 °C. The drop in iron content is caused by solidification of β-Al_5FeSi phase.

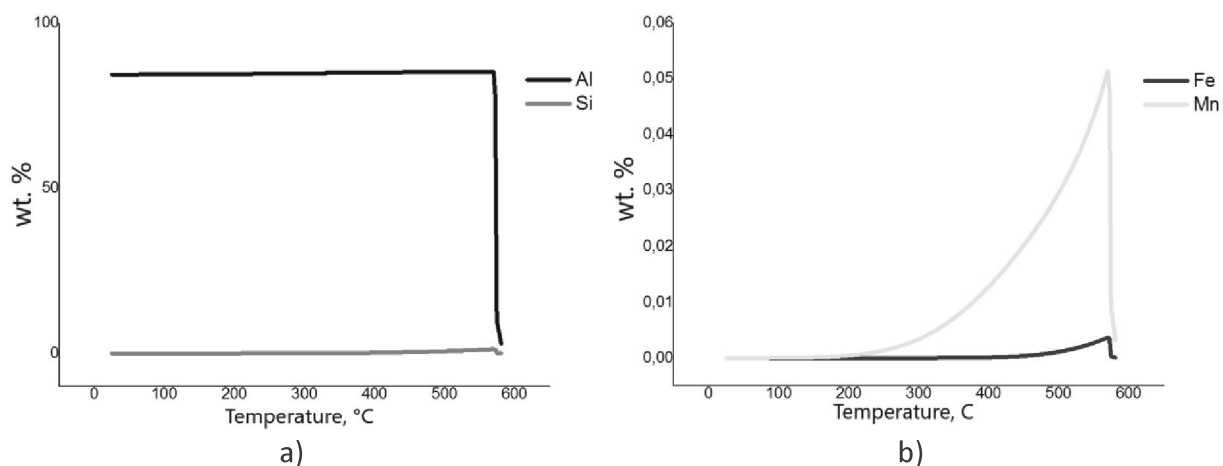The amount of components in α_{Al} is given in Figure 6, a and b.

a)   b)

Figure 6. The component ratio in α_{Al} solid solution:
a) Al and Si, b) Fe and Mn

The average amount of aluminum in α_{Al} solid solution reaches maximum value of 85.22 wt. % at 570 °C and remains constant till the end of solidification sequence. The maximum average amount of silicone in α_{Al} solid solution is 1.27 wt. % at 572 °C. At the end of solidification sequence the average value of silicone in α_{Al} solid solution drops to $4.76 \cdot 10^{-4}$ wt. %. The solid solubility of manganese in α_{Al} solid solution reaches its maximum of 0.05 wt. % at 570 °C, and drops significantly to $3.23 \cdot 10^{-7}$ wt. %. The maximum solid solubility of iron in α_{Al} solid solution is 0.004 wt. % at 570 °C. At the end of solidification sequence the amount of iron in α_{Al} solid solution is $1.75 \cdot 10^{-10}$ wt. %.

Elements amount in α-$Al_{15}(FeMn)_3Si_2$ phase in correlation to the temperature are shown in Figure 7.
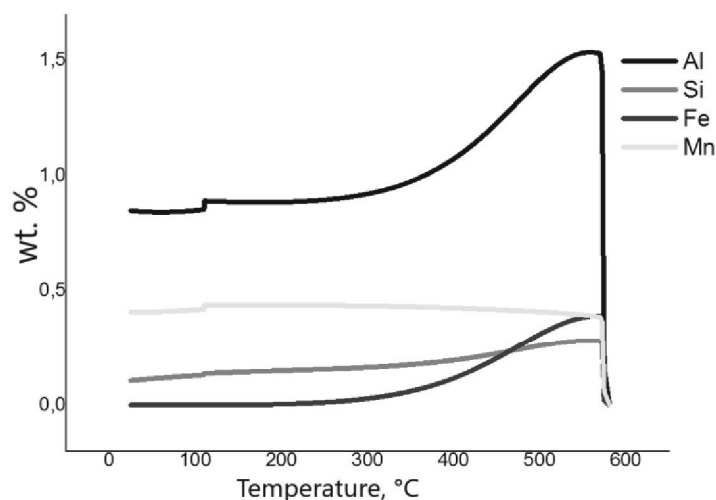
Figure 7. The solid solubility of Al, Si, Fe and Mn in α-Al$_{15}$(FeMn)$_3$Si$_2$ phase

The starting average content of aluminum is 0.023 wt. % and silicone is 0.005 wt. % in α-Al$_{15}$(FeMn)$_3$Si$_2$ phase at 580 °C respectively. The maximum amount of aluminum is 1.53 wt. % and silicone is 0.28 wt. % at 570 °C. Towards the end of solidification α-Al$_{15}$(FeMn)$_3$Si$_2$ phase contains average 0.85 wt. % of aluminum and 0.11 wt. % of silicone. The maximum iron content of 0.39 wt. % is reached at 570 °C. At the end of solidification sequence amount of iron drops slowly and reaches average amount of $2.61 \cdot 10^{-6}$ wt. %. The maximum manganese amount of 0.39 wt. % in α-Al$_{15}$(FeMn)$_3$Si$_2$ phase is achieved at 570 °C. The amount of manganese remains constant till the temperature of 110 °C. At the temperature of 110 °C the average amounts of aluminum (0.85 wt. %), silicone (0.13 wt. %) and manganese (0.41953 wt. %) slightly drop.
The amount of components in β-Al$_5$FeSi phase is given in Figure 8.

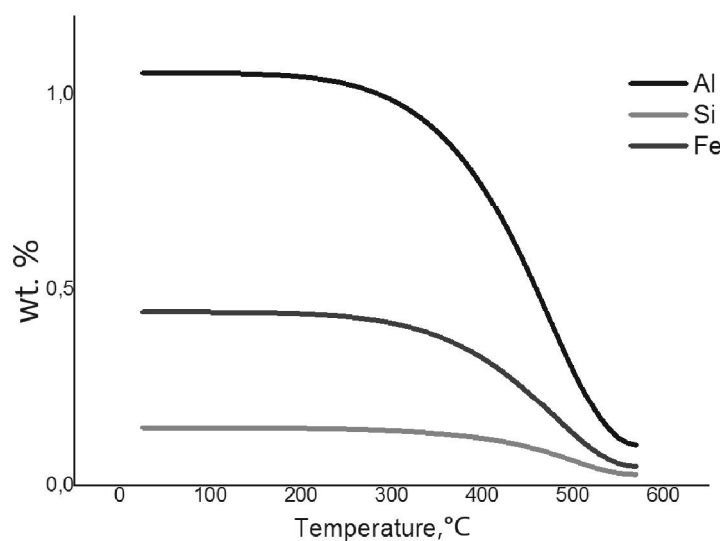Figure 8. The solid solubility of Al, Si, Fe and Mn in β-Al$_5$FeSi phase

The starting average content of aluminum is 0.10 wt. % and silicone is 0.029 wt. % in β-Al_5FeSi phase at 570 °C respectively. At the end of solidification β-Al_5FeSi phase contains in average 1.053 wt. % of aluminum and 0.146 wt. % of silicone. The average content of iron in α phase grows from starting 0.048 wt. % to 0.443 wt. % at the end of solidification sequence. The manganese content is not influenced by solidification of β-Al_5FeSi phase.

Decrease in the aluminum and silicone content in L is caused by transformation of α_{Al} dendritic network at 581 °C followed by solidification of α-$Al_{15}(FeMn)_3Si_2$ at 580 °C. The amount of aluminum is reduced additionally by solidification of β-Al_5FeSi phase at 570 °C. The reduction of manganese amount in L is caused by α-$Al_{15}(FeMn)_3Si_2$ solidification at 580 °C. Although the amount of iron begins to drop during solidification of α-$Al_{15}(FeMn)_3Si_2$, the more significant loss is noticed at 570 °C during β-Al_5FeSi phase solidification. Both aluminum and silicone content in α_{Al} solid solution stay unaffected till the end of solidification. The amounts of iron and manganese in α_{Al} solid solution are depleted during α-$Al_{15}(FeMn)_3Si_2$ and β-Al_5FeSi phase solidification, respectively. The amounts of aluminum, silicone and iron in α-$Al_{15}(FeMn)_3Si_2$ are reduced by solidification of β-Al_5FeSi phase. The manganese amount is unaffected by β-Al_5FeSi phase solidification. However, the amounts of aluminum and manganese are reduced in α-$Al_{15}(FeMn)_3Si_2$ phase after 110 °C due to the precipitation of $Al_{16}Mn_3Ni$. The β-Al_5FeSi phase grows till the end of solidification sequence.

The microstructure of the samples at the magnification of 500 X is given in Figure 9.
The results of light microscopy indicated the presence of Fe-rich intermetallic phases in Chinese script (Figure 9 a), transitional (Figure 9 b) and polyhedral morphology (Figure 9c). The intermetallic phases in needle-like morphology were not detected. The intermetallic phases in Chinese script morphology envelopes α_{Al} dendritic network (Figure 9a). The intermetallic phases with transitional morphology can be found at the border α_{Al} /β_{Si} (Figure 9b). The phases with polyhedral morphology are surrounded by eutectic (α_{Al} + β_{Si}) (Figure 9c).
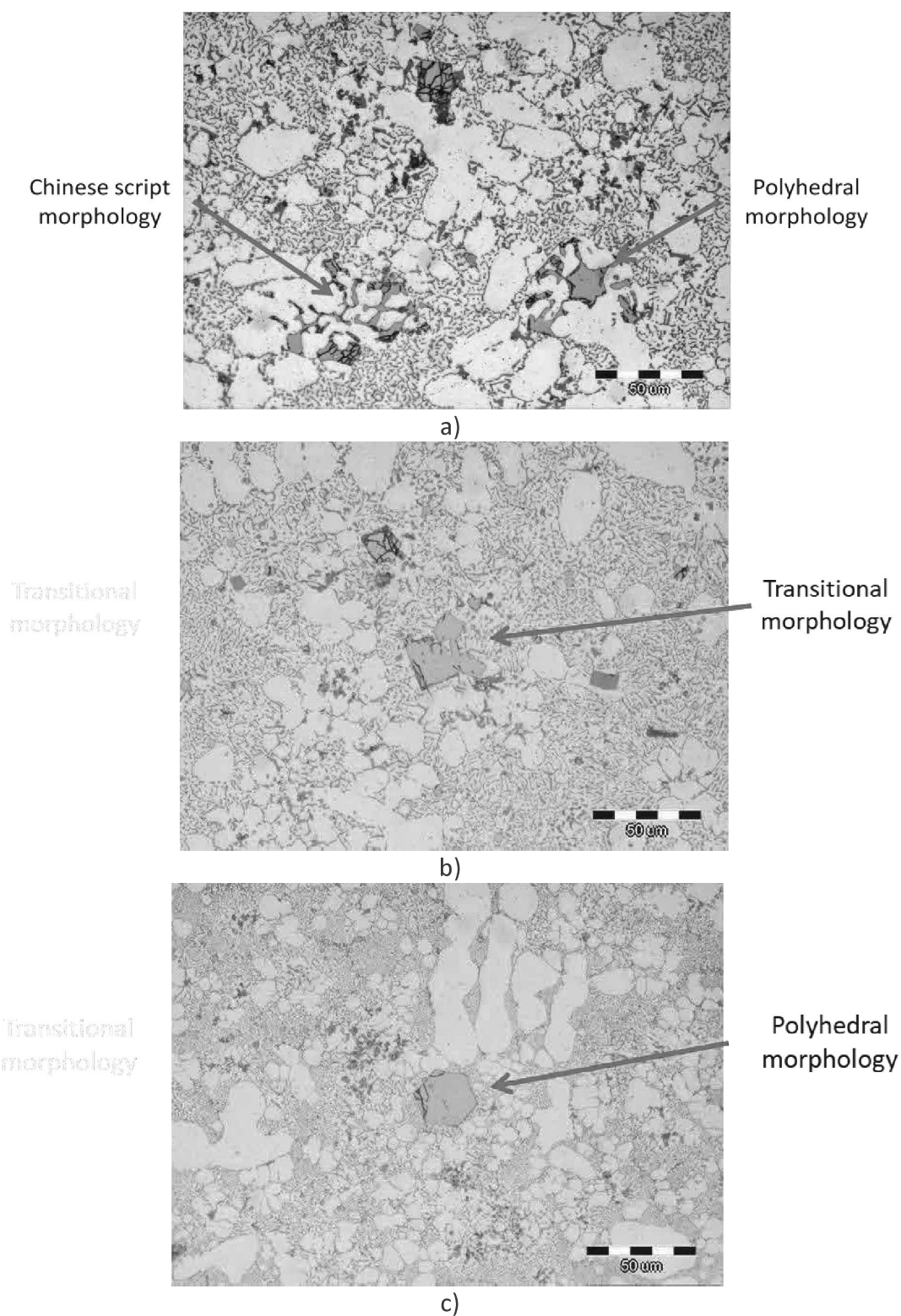
Figure 9. Microstructure of the samples showing: a) Chinese script morphology,
b) Transitional morphology, c) Polyhedral morphology

The BSE images of intermetallic phases in Chinese script and polyhedral morphology with corresponding EDS analysis are given in Figure 10.

Al - 59.91 wt.%
Si - 7.10 wt.%
Fe - 12.90 wt.%
Mn - 18.00 wt.%

Al - 63.21 wt.%
Si - 5.18 wt.%
Fe - 12.34 wt.%
Mn - 17.09 wt.%

a)   b)

Al - 59.53 wt.%
Si - 7.32 wt.%
Fe - 13.26 wt.%
Mn - 18.39 wt.%

Al - 60.88 wt.%
Si - 8.92 wt.%
Fe - 11.46 wt.%
Mn - 17.16 wt.%
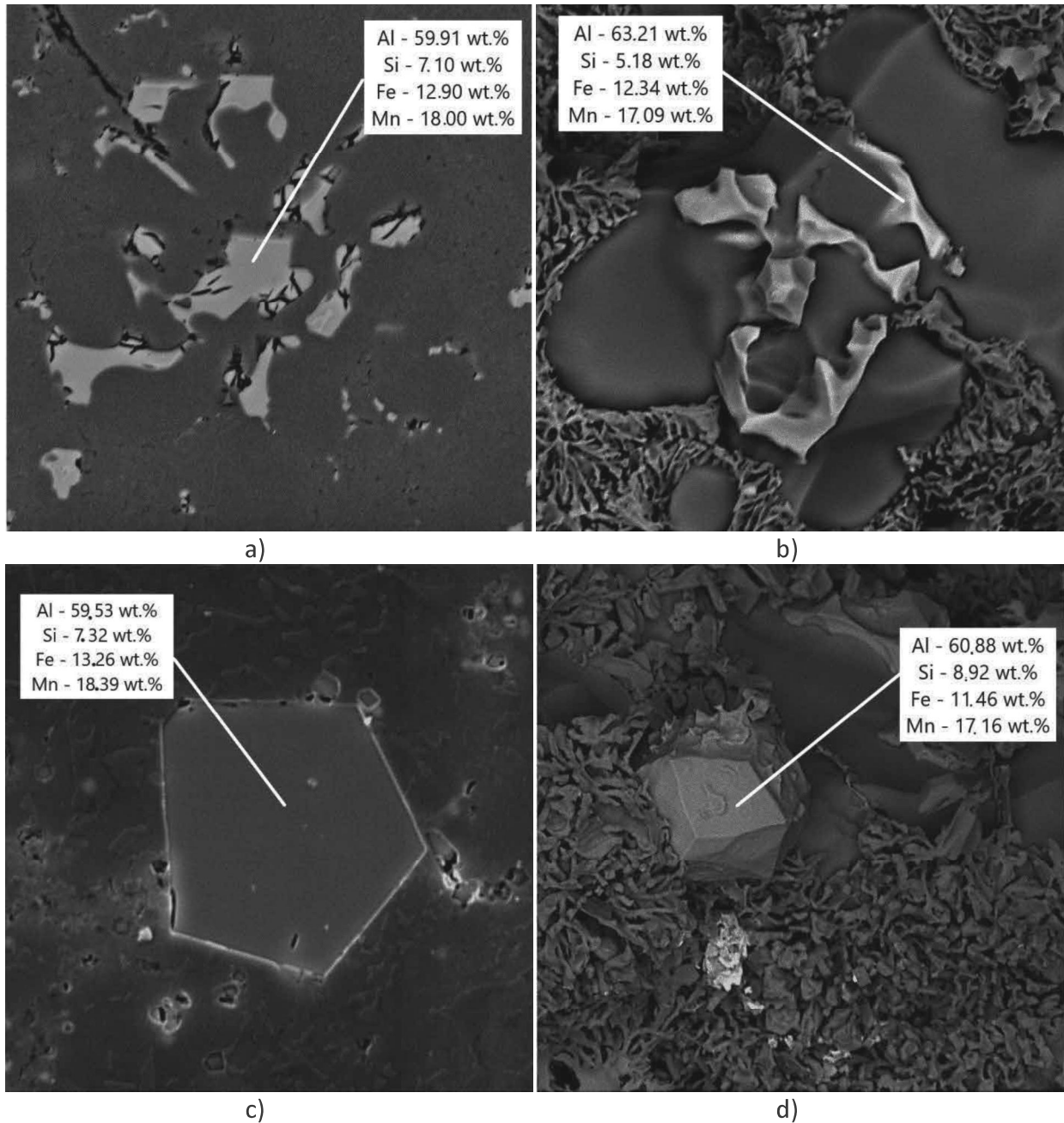
c)   d)

Figure 10. The SEI of:
a) Intermetallic phase in Chinese script morphology,
b) Intermetallic phase in Chinese script morphology after caustic chemical etching,
c) Intermetallic phase in polyhedral morphology,
d) Intermetallic phase in polyhedral morphology after caustic chemical etching

The Chinese script morphology of intermetallic phases is not typical (Figure 10a). The branches of intermetallic phase with Chinese script morphology surround α_{Al} dendritic network (Figure 10b). The polyhedral iron morphology is more compact (Figure 10c). The intermetallic phase in polyhedral morphology is surrounded by main eutectic (α_{Al} + β_{Si}) (Figure 10d).

The results of EDS analysis performed on intermetallic phases in Chinese script and polyhedral morphology are shown in Figure 11.
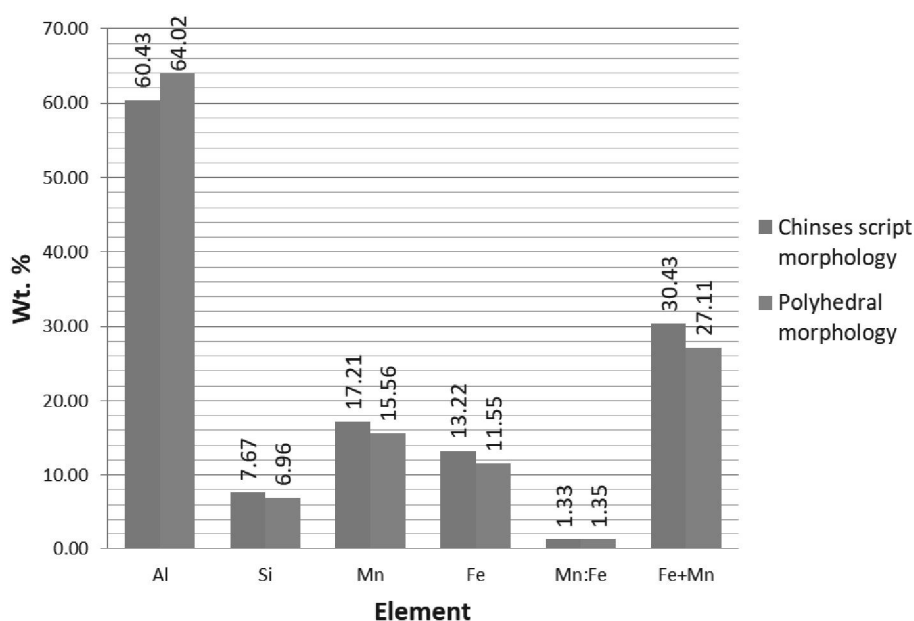

Figure 11. The average wt. % of elements in intermetallic phases in Chinese script and polyhedral morphology

The results shown in Figure 10 indicate small difference in average content of elements between intermetallic phases in Chinese script and polyhedral morphology. The intermetallic phases in Chinese script morphology have higher average amount of silicone, manganese, and iron. The total amount Fe + Mn is higher for Chinese script morphology, while polyhedral morphology has higher w (Mn/Fe).

The aluminum, silicone, manganese, iron wt. % as well as w (Mn/Fe) and total amount Mn + Fe for intermetallic phases in Chinese script and polyhedral morphology are given in Table 5.

Table 5. Results of EDS analysis of intermetallic phases in Chinese script and polyhedral morphology

Element, wt.%	Chinese script morphology		Polyhedral morphology	
	Mid value	Standard deviation	Mid value	Standard deviation
Al	64.02	6.10	60.43	1.39
Si	6.96	1.31	7.67	2.17
Fe	11.55	2.12	13.22	1.37
Mn	15.56	2.81	17.21	2.68
Mn/Fe	1.35	0.04	1.33	0.27
Fe + Mn	27.11	4.91	30.43	1.63

The intermetallic phases in Chinese script morphology contain: 64.02 wt. % of aluminum, 6.96 wt. % of silicone, 11.55 wt. % of iron and 15.65 wt. % of manganese. The Mn/Fe ratio is 1.35, while the Mn + Fe is 27.11. The intermetallic phases with polyhedral morphology contain: 60.43 wt. % of aluminum, 7.67 wt. % of silicone, 13.22 wt. % of iron and 17.21 wt. % of manganese. The Mn/Fe ratio in polyhedral shaped intermetallics is 1.33 while Fe + Mn total is 30.43. The intermetallic phases in Chinese script morphology have higher Al content. The content of silicone, iron and manganese is higher in polyhedral shaped intermetallic. The Mn/Fe ratio and Fe + Mn are higher in polyhedral intermetallics.

CONCLUSIONS

The transformation and solidification of Fe-rich intermetallic phases during solidification sequence of AlSi12 alloy with w (Mn/Fe) ratio of 0.99 were investigated.

The equilibrium solidification calculations comprehended solidification of α-$Al_{15}(FeMn)_3Si_2$ and β-Al_5FeSi Fe-rich intermetallic phases. The solidification sequence begins with transformation of α_{Al} dendritic network at 581 °C followed by solidification of eutectic α-$Al_{15}(FeMn)_3Si_2$ from the L at 580 °C. The eutectic (α_{Al} + β_{Si}) solidifies from the L at 574°C. The β-Al_5FeSi phase solidifies at 570 °C reducing the amount of α-$Al_{15}(FeMn)_3Si_2$. The additional reduction in α-$Al_{15}(FeMn)_3Si_2$ phase content occurs at 110 °C during precipitation of $Al_{16}Mn_3Ni$.

Under realistic conditions the solidification sequence begins with solidification of primary Al_3Fe, $Al_6(FeMn)$ and α-Al_8Fe_2Si Fe-intermetallic phases. The solidification of α-$Al_{15}(FeMn)_3Si_2$ phase involves peritectic reaction between L, Al_3Fe and $Al_6(FeMn)$ at 648 °C. The β-Al_5FeSi phase solidifies in the interval of 597 °C to 607 °C during peritectic reaction engaging L and α-Al_8Fe_2Si.

The intermetallic phases with Chinese script and polyhedral morphology were identified by light microscopy. The β-Al_5FeSi phase in needle-like morphology was not found.

The EDS analysis indicated similarities between intermetallic phases with Chinese script and polyhedral morphology. The indicated similarity in chemical composition points towards the

high w (Mn/Fe) ratio. The w (Mn/Fe) ratio of 0.99 enabled solidification of α-$Al_{15}(FeMn)_3Si_2$ phase in polyhedral morphology.

Acknowledgements

REFERENCES

[1] S. Seifeddine, S. Johansson, I. L. Svensson, The influence of cooling rate and magnesium content on the β-Al5FeSi phase formation and mechanical properties of Al-Si – based alloys, Materials Science and Engineering A, 490(2008)1-2, pp. 385-390.

[2] L. Hurtalová, E Tillová, M. Chalupová, E. Ďuriníková, Effect of chemical composition of secondary al-si cast alloy on intermetallic phases, Scientific Proceedings IX International Congress "Machines, Technologies, Materials", Scientific Technical Union of Mechanical Engineering, 19th-21th of September, Varna, Bulgaria, pp. 23-26.

[3] L. Hurtalová, J. Belan, E. Tillová, M. Chalupová, Changes in structural characteristics of hypoeutectic Al-Si cast alloy after age hardening, Materials Science, 18(2012)3, pp. 228-233.

[4] S. Gowri and F. H. Samuel, Effect of alloying elements on the solidification characteristics and microstructure of Al-Si-Cu-Mg-Fe 380 alloy, Metallurgical and Materials Transactions A, 25(1994)2, pp. 437-448.

[5] J. G. Kaufman, E. L. Rooy, Aluminum Alloy Castings: Properties, processes, and applications, ASM International, Peoria, 2004.

[6] S. Belmares-Perales, M. Castro-Román, M. Herrera-Trejo, and L. E. Ramírez-Vidaurri, Effect of cooling rate and Fe/Mn weight ratio on volume fractions of α-AlFeSi and β-AlFeSi phases in Al–7.3Si–3.5Cu alloy, Metals and Materials International, 14(2008)3, pp. 307-314.

[7] R. S. Rana, R. Purohit, S. Das, Reviews on the influences of alloying elements on the microstructure and mechanical properties of aluminum alloy composites, International Journal of Scientific and Research Publications, 2(2012)6, pp. 2250-3153.

[8] M. M. Makhlouf, D. Apelian, L. Wang, Microstructures and properties of aluminum die casting alloys, North American Die Casting Association, Rosemont, 1998.

[9] C. Puncreobutr, A. B. Phillion, J. L. Fife, P. Rockett, A. P. Horsfield, P. D. Lee, In situ quantification of the nucleation and growth of Fe-rich intermetallics during Al alloy solidification, Acta Materialia, 79(2014)1, pp. 292-303.

[10] J. Shouxun, Y. Wenchao, F. Gao, D. Watson, Z. Fan, Effect of iron on the microstructure and mechanical property of Al–Mg–Si–Mn and Al–Mg–Si diecast alloys, Materials Science & Engineering A, 564(2013)1, pp. 130-139.

[11] G. B. Winkelman, Z. W. Chen, D. H. StJohn, M. Z. Jahedi, Morphological features of interfacial intermetallics and interfacial reaction rate in Al-11Si-2.5Cu-(0.15/0.60)Fe cast alloy/die steel couples, Journal of Materials Science, 39(2004)1, pp. 519-528.

[12] S. Ji, W. Yang, F. Gao, D. Watson, Z. Fan, Effect of iron in Al-Mg-Si-Mn ductile die cast alloy, Light Metals 2013, Springer, Cham, 2013.

[13] K. A. Nazari, S. G. Shabestari, Effect of micro alloying elements on the interfacial reactions between molten aluminum alloy and tool steel, Journal of Alloys and Compounds, 478(2009), pp. 523-530.

[14] C. H. Cáceres, I. L. Svensson, J. A. Taylor, Strength-Ductility Behaviour of Al-Si-Cu-Mg Casting Alloys in T6 Temper, International Journal of Cast Metals Research, 15(2003)5, pp. 531-543.

[15] M. Pokusová, I. Berta, M. Murgašová, Metallurgical processing of Al-Si alloys with increased iron content using sodium, strontium, and tellurium, Journal of Casting & Materials Engineering, 2(2019)1, pp. 9-13.

[16] H. W. L. Phillips, Annotated equilibrium diagrams of some aluminium alloy systems, Institute of Metals, Michigan, 1959.

[17] M. W. Meredith, A. L. Greer, P. V. Evans, R. G. Hamerton, The generation of Al_mFe in ductile aluminium alloys with different grain refining additions, Light Metals 1998, The Minerals, Metals & Materials Society, 1998.

[18] A. Aliravci, M. Pekgüleryüz, Calculation of phase diagrams for the metastable Al-Fe phases forming in direct-chill (DC)-cast aluminum alloy ingots, Calphad, 22(1998)2, pp. 147-155.

[19] C. A. Aliravci, J. E. Gruzleski, M. Pekgiileryuz, A thermodynamic study of metastable Al-Fe phase formation in direct chill (DC)-cast aluminum alloy ingots, Light Metals 1998, The Minerals, Metals & Materials Society 2016, 1998.

[20] Z. K. Liu, Y. A. Chang, Thermodynamic assessment of the Al-Fe-Si system, Metallurgical and Materials Transactions A, 30A(1999), pp. 1081-1095.

[21] M. Gnatko, C. Li, A. Arnold, B. Friedrich, Purification of aluminium cast alloy melts through precipitation of Fe-containing intermetallic compounds, Metals, 8(2018)10, pp. 796-808.

[22] N. A. Belov, D. G. Eskin, A. A. Aksenov, Multicomponent phase diagrams: Application for commercial aluminum alloys, Elsevier Science, 2005.

[23] S. Ji, W. Yang, F. Gao, D. Watson, Z. Fan, Effect of iron on the microstructure and mechanical property of Al–Mg–Si–Mn and Al–Mg–Si diecast alloys, Materials Science & Engineering A, 564(2013)1, pp. 130-1390.

[24] J. Roger, E. Jeanneau, J. C. Viala, Crystal structure of the ternary compound γ-Al3FeSi, Zeitschrift für Kristallographie Crystalline Materials, 226(2011)11, pp. 805-813.

[25] N. A. Belov, A. A. Aksenov, D. G. Eskin, Iron in Aluminum Alloys, Taylor & Francis Group, London, 2002.

[26] G. Effenberg, S. Ilyenko, Light metal ternary systems: phase diagrams, crystallographic and thermodynamic data, Springer, Berlin, 2005.

[27] X. Cao, J. Campbell, Morphology of β-Al$_5$FeSi phase in Al-Si cast alloys, Materials Transactions, 47(2006)5, pp. 1303-1312.

[28] M. Mahta, M. Emamy, A. Daman, A. Keyvani, J. Campbell, Precipitation of Fe rich intermetallics in Cr- and Co-modified A413 alloy, International Journal of Cast Metals Research, 18(2005)2, pp. 73-79.

[29] X. Cao and J. Campbell, The Solidification characteristics of Fe-rich intermetallics in Al-11.5Si-0.4Mg cast alloys, Metallurgical and Materials Transactions A, 35(2004)5, pp. 1425-1435.

[30] M. Warmuzek, J. Sieniawski, K. Wicher, G. Mrowka, The study of the distribution of the transition metals and Si during primary precipitation of the intermetallic phases in Al–Mn–Si alloys, Journal of Materials Processing Technology, 175(2006)1, pp. 421-426.

[31] M. Mahta, M. Emamy, X. Cao, J. Campbell, Overview of β-Al$_5$EeSi phase in Al-Si alloys, Materials Science Research Trends, Nova Science Publishers Inc., Ontario , 2008.

[32] C. Puncreobutr, D. P. Lee, K. M. Kareh, T. Connelley, J. L. Fife, A. B. Philion, Influence of Fe-rich intermetallics on solidification defects in Al-Si-Cu alloys, Acta Materialia, 68(2014)1, pp. 42-51.

[33] J. Z. Yi, Y. X. Gao, P. D. Lee, T. C. Lindley, Effect of Fe-content on fatigue crack initiation and propagation in a cast aluminum–silicon alloy (A356–T6), Materials Science and Engineering A, 386(2004)1, pp. 396-407.

[34] L. Lu and A. K. Dahle, Iron-rich intermetallic phases and their role in casting defect formation in hypoeutectic Al-Si alloys, Metallurgical and Materials Transactions A, 36A(2005)1, pp. 819-835.

[35] N. Roy, A. M. Samuel, F. H. Samuel, Porosity formation in Al-9 wt. % Si-3 wt. % Cu alloy systems: metallographic observations, Metallurgical and Materials Transactions A, 27(1996)2, pp. 415-429.

[36] C. M. Dinnis, J. A. Taylor, A. K. Dahle, Interactions between iron, manganese, and the Al-Si eutectic in hypoeutectic Al-Si alloys, Metallurgical and Materials Transactions A, 37(2006)11, pp. 3283-3291.

[37] S. G. Shabestari, S. Ghodrat, Assessment of modification and formation of intermetallic compounds in aluminum alloy using thermal analysis, Materials Science and Engineering A, 467(2007)1, pp. 150-158.

[38] C. Bidmeshki, V. Abouei, H. Saghafian, S. G. Shabestari, M. T. Noghani, Effect of Mn addition on Fe-rich intermetallics morphology and dry sliding wear investigation of hypereutectic Al-17.5%Si alloys, Journal of Materials Research and Technology, 5(2016)3, pp. 250-258.

273

[39] T. Gao, K. Hu, L. Wang, B. Zhang, X. Liu, Morphological evolution and strengthening behavior of α-Al(Fe,Mn)Si in Al–6Si–2Fe–xMn alloys, Results in Physics, 7(2017)1, pp. 1051-1054.

[40] A. Darvishi, A. Maleki, M. M. Atabaki, M. Zargami, Mutual effect of iron and manganese on microstructure and mechanical properties of aluminium-silicon alloy, Metallurgical & Materials Engineering, 16(2010)1, pp. 11-24.

[41] Z. Zhang, H. Tezuka, E. Kobayashi, T. Sato, Effects of the Mn/Fe ratio and cooling rate on the modification of Fe intermetallic compounds in cast A356 based alloy with different Fe contents, Materials Transactions, 54(2013)8, pp. 1484-1490.

THE EFFECT OF ANNEALING TIME ON MICROSTRUCTURE AND IMPACT ENERGY OF STAINLESS STEEL AISI 316L

Stjepan Kožuh[1*], Katarina Pavičić[2], Ivana Ivanić[1], Milan Bizjak[3], Mirko Gojić[1]

[1] University of Zagreb Faculty of Metallurgy, Sisak, Croatia
[2] Master degree student at University of Zagreb Faculty of Metallurgy, Sisak, Croatia
[3] University of Ljubljana Faculty of Natural Sciences and Engineering, Ljubljana, Slovenia

Abstract

In this work the results of microstructural analysis and impact energy testing of austenitic stainless steel AISI 316L were carried out. Investigations were performed before and after annealing at 850 °C. Annealing time in this investigation varied from 30 to 90 minutes. After annealing, the samples were cooled in room temperature air. Microstructural analysis of initial rolled and different annealed states was performed by optical microscopy (OM) and scanning electron microscopy (SEM) equipped with device for energy dispersive spectroscopy (EDS). Impact tests were performed on Charpy V-notch specimens at room temperature. Initial rolled state of investigated steel showed the presence of typical elongated polygonal grains austenite and delta ferrite while annealed states showed the presence and evolution of sigma phase in microstructure. Impact energy value of initial rolled state was 260 J and by increasing annealing time it decreases.

Keywords: _stainless steel, microstructure, heat treatment, annealing, impact energy_

*Corresponding author _(e-mail address): kozuh@simet.hr_

INTRODUCTION

Stainless steels (SS) are based on the binary Fe-Cr systems, the properties of which are modified by the additional alloying elements like nickel, molybdenum and manganese. Molybdenum is added usually to type 316 steel to enhance the corrosion properties, primarily the pitting and crevice corrosion resistance [1]. In the world`s total stainless steel production austenitic type steels take about 60% [2]. Austenitic stainless steels are often used in nuclear power plants, boilers, heat exchangers, chemical reactors etc. because their

high resistance to corrosion and high temperature [3-5]. Also, stainless steel offers exceptional advantages for applications in construction [6]. Mostly stainless steels are used for construction as flat products and bars. Besides acceptable yield strength and tensile strength austenitic stainless steels are characterized by high impact energy and relatively low hardness. When considering the operational performance of austenitic stainless steel, the most important points to be taken into account are corrosion resistance, mechanical properties and the integrity of the welded joint in the case of welding these steels. Their high corrosion resistance resulted from formation of a continuous and protective surface oxide layer (passive film). This film is only a few nanometers thick and enriched in Cr (III) oxide/hydroxide species.

To reduce or prevent of microfissures in austenitic stainless steel, a minimum delta ferrite is required. Beneficial effect of delta ferrite is in dissolving more of harmful elements such as sulfur, phosphorus and boron in austenite [7]. But, this ferrite can be transformed in sigma phase. Austenitic steels may undergo microstructural changes when they are exposed to elevated temperature for a shorter or longer period of time. Microstructural variations caused by heat treatment are responsible for changes in the mechanical properties and corrosion resistance. Usually, three intermetallic phases which can be occurred in austenitic stainless steels are sigma phase, chi phase and Laves phase [8-10]. The precipitation mechanism in austenitic stainless steels has been the subject of many investigations motivated by the detrimental effects of the precipitated phases on impact energy and corrosion resistance of steels [11-13]. Padilha et al. [11] and Sourmail [13] reported the precipitation of carbides ($M_{23}C_6$, MC, M_6C, M_7C_3), primary nitrides (MN, M = Zr, Ti, Nb and V), and secondary nitrides (M_2N, M = Cr, Fe) in austenitic stainless steels during thermal treatment (annealing) or welding. Dománková et al. [10] mentioned the following sigma phase composition in AISI 316 which observed after ageing at 800 °C: 56–61%Fe, 21–26%Cr, 12–21%Mo and 1–5%Ni. As the sigma phase composition tends to vary it is difficult to define it by a formula but it is certain that it negatively affects on the steel properties.

The sigma phase has significant influence on properties of stainless steels and has been researched for some time [14]. Generally, the sigma phase forms via thermal ageing but also can be formed via radiation-induced segregation in FeCr alloys. Sigma phase is an intermetallic compound with a complex tetragonal crystalline structure and a typical sigma phase composition for the AISI 316L steel type is 44 % Fe - 29 % Cr - 8 % Mo. Sigma phase can be responsible for reduction in impact energy at room temperature.

Due to AISI 316L stainless steel can be particularly useful at very high temperatures (e.g. in nuclear reactor) it becomes important to study the material microstructure and impact energy at elevated temperatures. The aim of the present work is to show possibility the sigma phase appearance and whether relative short annealing time (up to 90 minutes) can have an influence on microstructure and impact energy of austenitic stainless steel AISI 316L.

MATERIALS AND METHODS

The material used in this study was AISI 316L type stainless steel which was delivered in hot rolled state. The chemical composition of the investigated steel is listed in Table 1. Specimens for investigation were produced from steel plates of 15 mm thickness. Austenitic stainless steel AISI 316L was studied before and after heat treatment. Heat treatment was consisted from annealing at 850 °C for 30, 60 and 90 minutes followed by cooling in the air. Microstructural analysis was carried out by optical microscopy Olympus GX 51 (OM) and scanning electron microscopy TESCAN VEGA 5136 MM (SEM) equipped with device for energy dispersive spectroscopy (EDS). Samples used for microstructural characterization were subsequently ground (papers grid 240-1200), polished (0.3 μ Al_2O_3) and electrolytically etched in two different solutions. To expose austenite boundaries the etching solution 1 containing 60 ml HNO_3 and 40 ml water solution was used at 1V DC for 20 s. Sigma phase were identified with etching solution 2 composed from 56 g KOH in 100 ml water at 2V DC for 10 s. Impact tests were performed on Charpy V-notch specimens (7.5x10x55 mm) at room temperatures on device MLF System PSW 300.

Table 1. Chemical composition of investigated austenitic stainless steel AISI 316L, wt.%

C	Mn	Si	Cu	V	Mo	Al	Cr	Ni	W	Ti	Nb	Fe
0.018	1.50	0.33	0.39	0.078	1.91	0.006	17.34	10.56	0.121	0.003	0.025	balance

RESULTS AND DISCUSSION

From the results of this paper it was possible to establish a correlation between the microstructure, impact energy and various annealing time at 850 °C for investigated AISI 316L stainless steel. The material in delivered (hot rolled) and thermal treated (annealed) state was microstructural characterized firstly after electrolytically etching to expose austenite boundaries (etching solution 1). Figures 1-3 show a typical microstructure of the austenitic stainless steel of the present study. Optical micrographs (Figure 1a) and SEM micrographs (Figures 2a and 3) of microstructure of rolled state exhibited typical elongated grains of polygonal austenite and delta ferrite. Stringers of delta ferrite are elongated in the direction of rolling. In AISI 300 series stainless steels, during casting firstly is formed delta ferrite, and then this ferrite transforms to austenite by diffusion of chromium and nickel between the phases. Chromium diffuses to the ferrite and nickel to the advancing austenite. The austenite grains nucleate and grow into delta ferrite grains. The presence of residual delta ferrite retained at room temperature can be ascribed to the slow diffusion of chromium and nickel. The microstructure, according to Schaeffler diagram (Figure 4) [15], consisted of austenite and up to 10% of delta ferrite because the Cr_{eq}/Ni_{eq} ratio was 1.69 (Equations 1 and 2).

$$Cr_{eq} = \%Cr + 1.5\%Si + \%Mo + 0.5\%(Ta+Nb) + 2\%Ti + \%W + \%V + \%Al \qquad (1)$$

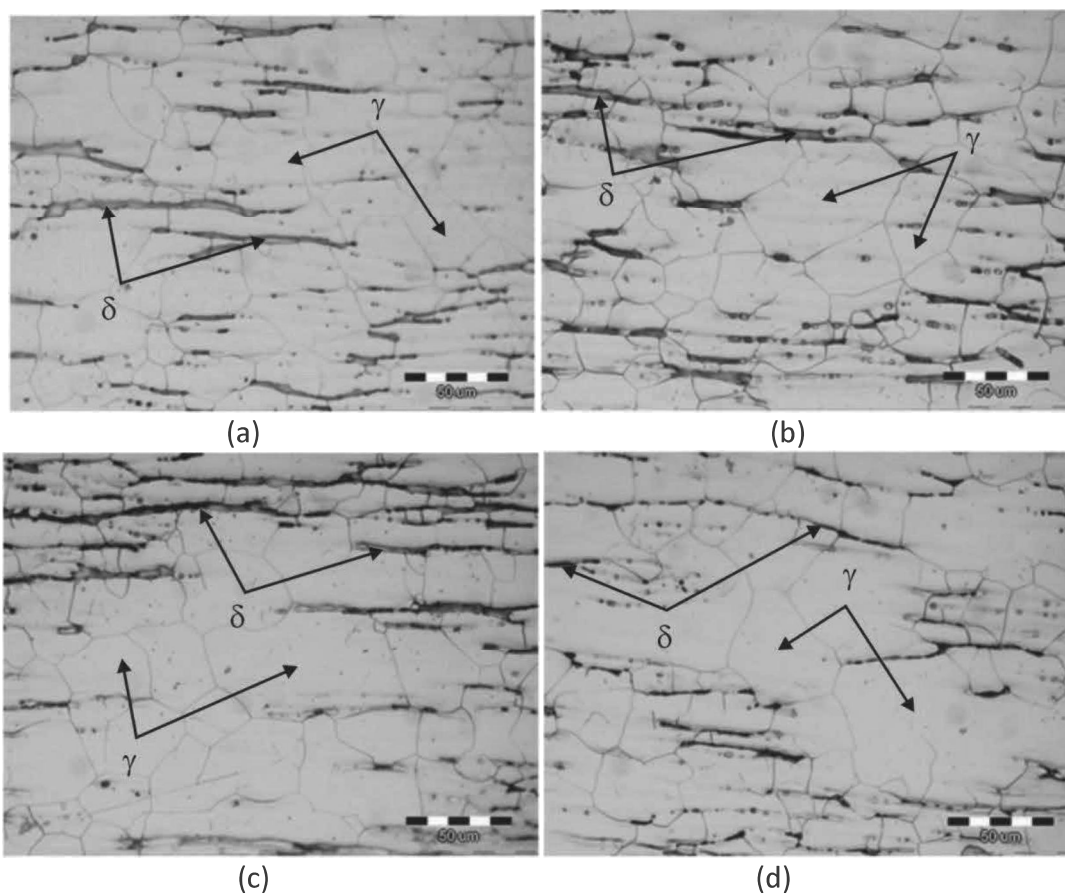$$Ni_{eq} = \%Ni + 30\%C + 0.5\%Mn + 0.5\%Co \qquad (2)$$

(a)

(b)

(c)

(d)

Figure 1. Optical micrographs of AISI 316L stainless steel in rolled (delivered) state (a), annealed state 850 °C/30 min (b), annealed state 850 °C/60 min (c), annealed state 850 °C/90 min (d); etching solution 1
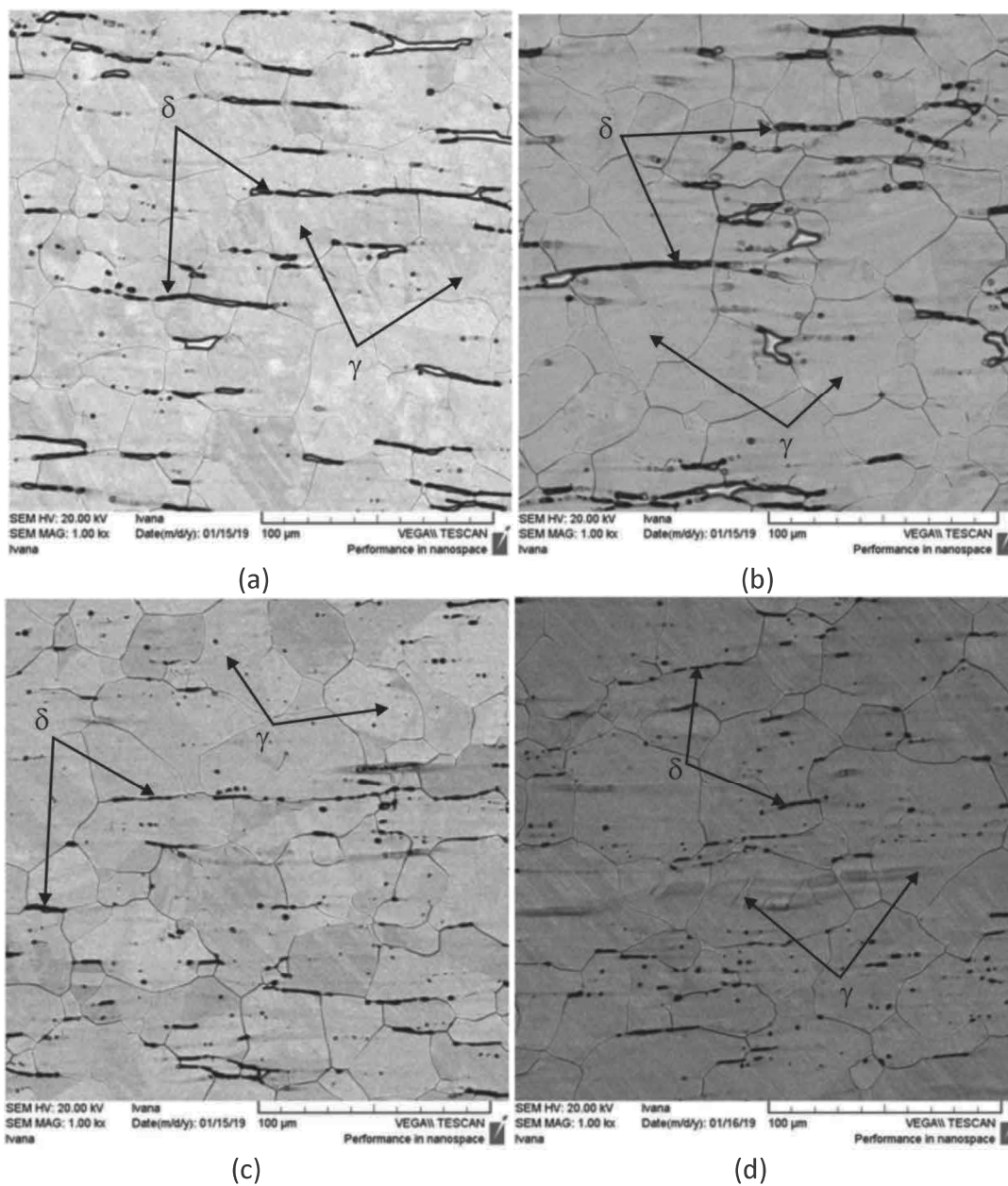
Figure 2. SEM micrographs of AISI 316L stainless steel in rolled (delivered) state (a), annealed state 850 °C/30 min (b), annealed state 850 °C/60 min (c), annealed state 850 °C/90 min (d); etching solution 1